PCCP

Accepted Manuscript

ROYAL SOCIETY OF CHEMISTRY

www.rsc.org/pccp

Journal Name

RSCPublishing

ARTICLE

Theoretical study of the oxidation mechanisms of naphthalene initiated by hydroxyl radicals: The O_2 addition reaction pathways

Cite this: DOI: 10.1039/x0xx00000x

Received 00th January 2012,
Accepted 00th January 2012

DOI: 10.1039/x0xx00000x

www.rsc.org/

A. Shiroudi,[a] M.S. Deleuze∗[a] and S. Canneaux[b]

Atmospheric oxidation of the naphthalene-OH adduct $[C_{10}H_8OH]^\bullet$ (R1) by molecular oxygen in its triplet electronic ground state has been studied using density functional theory along with the B3LYP, ωB97XD, UM05-2x and UM06-2x exchange-correlation functionals. From a thermodynamic viewpoint, the most favourable process is O_2 addition at the C_2 position in *syn* mode, followed by O_2 addition at the C_2 position in *anti* mode, O_2 addition at the C_4 position in *syn* mode, and O_2 addition at the C_4 position in *anti* mode, as the second, third and fourth most favourable processes. The *syn* modes of addition at these positions are thermodynamically favoured over the *anti* ones by the formation of an intramolecular hydrogen bond between the hydroxyl and peroxy substituents. Analysis of the computed structures, bond orders and free energy profiles demonstrate that the reaction steps involved in the oxidation of the naphthalene-OH adduct by O_2 satisfy Hammond's principle. Kinetic rate constants and branching ratios under atmospheric pressure and in the fall-off regime have been supplied, using transition state and RRKM theories. By comparison with experiment, these data confirm the relevance of a two-step reaction mechanism. Whatever the addition mode, O_2 addition in C_4 position is kinetically favoured over O_2 addition in C_2 position, in contrast with the expectations drawn from thermodynamics and reaction energies. Under a kinetic control of the reaction, and in line with the computed reaction energy barriers, the most efficient process is O_2 addition at the C_4 position in *syn* mode, followed by O_2 addition at the C_2 position in *syn* mode, O_2 addition at the C_4 position in *anti* mode, and O_2 addition at the C_2 position in *anti* mode as the second, third and fourth most rapid processes. The computed branching ratios also indicate that the regioselectivity of the reaction decreases with increasing temperatures and decreasing pressures.

1. Introduction

Aromatic hydrocarbons, including benzene and polycyclic aromatic hydrocarbons (PAHs), are present in gasoline and diesel fuels,[1–4] and are released into the atmosphere principally during incomplete combustion.[5,6] PAHs with two to three rings are mainly in the gas phase under atmospheric conditions.[7,8] These compounds chemically react with tropospheric gases such as ozone, nitrate radicals, and hydroxyl radicals.[9,10] The reactions with these radicals are usually the most important sink reactions of organic compounds in the atmosphere.[11,12] The oxidation of aromatic rings by OH radicals in the gas phase under ambient conditions yields hydroxycyclohexadienyl-type radicals, which can back decompose to the reactants or react further with NO_2 or O_2 to yield highly carcinogenic derivatives.[13-22] Under ambient atmospheric conditions, including severely polluted urban areas, it is known that the reactions of OH-monocyclic aromatic hydrocarbon adducts with O_2 dominate.[19]

In two preceding articles,[23,24] we have studied the first reaction steps involved in the oxidation pathways of naphthalene, the most volatile and abundant PAH in polluted urban areas, by OH radicals. Whereas the H abstraction pathway at high temperatures ($T \geq 600$ K) yields 1- and 2-naphthyl radicals, the OH addition pathway which dominates under inert (He) conditions at low temperatures ($T \leq 410$ K) leads to 1- and 2-naphthol. Under atmospheric conditions, however, the intermediate energized adduct $[C_{10}H_8OH]^\bullet$ (R1) involved in the latter reaction is expected to react primarily with triplet molecular oxygen, to form $[C_{10}H_8OH]^\bullet$-O_2 peroxy radicals (R2). O_2 addition onto the R1 energized adduct can occur at five different positions, i.e. onto the C_2, C_4, C_5, C_7, and C_9-positions (Figure 1). Depending on the relative (*syn* or *anti*) location of the hydroxyl and peroxy substituents with respect to the attacked phenyl ring scaffold, this third reaction step leads on total to 10 different isomers (Figure 1), which may be referred, as in a previous study by Zhang *et al*.[25] to as the R1-*i*OO-*anti*/*syn* (*i* = 2, 4, 5, 7, 9) radicals. Similar reactions of O_2 with [OH-benzene]$^\bullet$ [26–29] and [OH-toluene]$^\bullet$ [30] adducts are known to proceed through a reversible addition of O_2 to the OH-aromatic adduct to form an OH-aromatic-O_2 peroxy radical.[22]

Koch *et al*.[22,31–33] have experimentally studied the gas-phase reaction between O_2 and naphthalene-OH radical at 298, 336 and 400 K, by means of flash photolysis/resonance fluorescence (FP/RF). The reported rate constants for the reactions of naphthalene-OH radical with O_2 at 400 K are less than 10^{-17} cm^3 molecule^{-1}s^{-1}, in accordance with the negative temperature dependence observed in the experiments at 336 and 298 K[31,33] resorting to chemical cycling of radicals.[32,34] Experimental studies of the gas-phase reaction between O_2 and naphthalene-OH radicals are

extremely difficult and challenging, and still badly need theoretical modelling for reliable enough insights into the reaction mechanisms.

In a recent theoretical study, Zhang *et al.*[25] investigated the reactions of the energized adduct R1 with molecular oxygen in its triplet electronic ground state, upon considering addition of O_2 in both the *syn* (same side) and *anti* (opposite side) positions with respect to the OH substituent and to the plane defined by the carbon backbone in the adduct (Figure 1). According to their results, it was found that the thermodynamically most favourable reaction consists in addition of O_2 onto R1 at the C_2 position (Figure 1) and in the *anti* mode, thus with the OH and O_2 substituents lying on opposite sides of the carbon backbone in the peroxy radical. This conclusion is however quite surprising, because one would intuitively expect that addition at the C_2 position in the *syn* mode should be thermodynamically favoured by the formation of an intramolecular hydrogen bonding between the terminal oxygen of the peroxy (O_2) group and the hydrogen of the OH group – an observation which led us to undertake a detailed verification of the study by Zhang *et al.*[25]

In addition to the work by Zhang *et al.*[25] we also wish to supply detailed computations of kinetic rate constants for all reaction steps involved in the addition of O_2 onto R1, as well as effective rate constants for the whole process at various temperatures and pressures. In this purpose, use shall be made of transition state theory (TST)[35–44] and statistical Rice-Ramsperger-Kassel-Marcus (RRKM)[43–45] theory, in conjunction with the popular B3LYP (Becke-3-parameters-Lee-Yang-Parr) functional,[46,47] but also the dispersion-corrected ωB97XD functional,[48] as well as the UM05-2x[49] and UM06-2x[49,50] functionals which have been specifically designed for accurate studies of chemical reactions, both from a thermodynamic and kinetic viewpoint. For the sake of reliability and accuracy, use shall also be made of Dunning's augmented correlation consistent polarized valence basis set of triple zeta quality (aug-cc-pVTZ).[51] This basis set is about twice as large as the 6-311+G(2df,p) basis set that was employed by Zhang *et al.*[25]

In the present work, we also strive to supply further chemical insights into the reaction mechanisms, by analyzing results in terms of natural bond orbital (NBO) occupancies,[52,53] and donor-acceptor interaction energies.

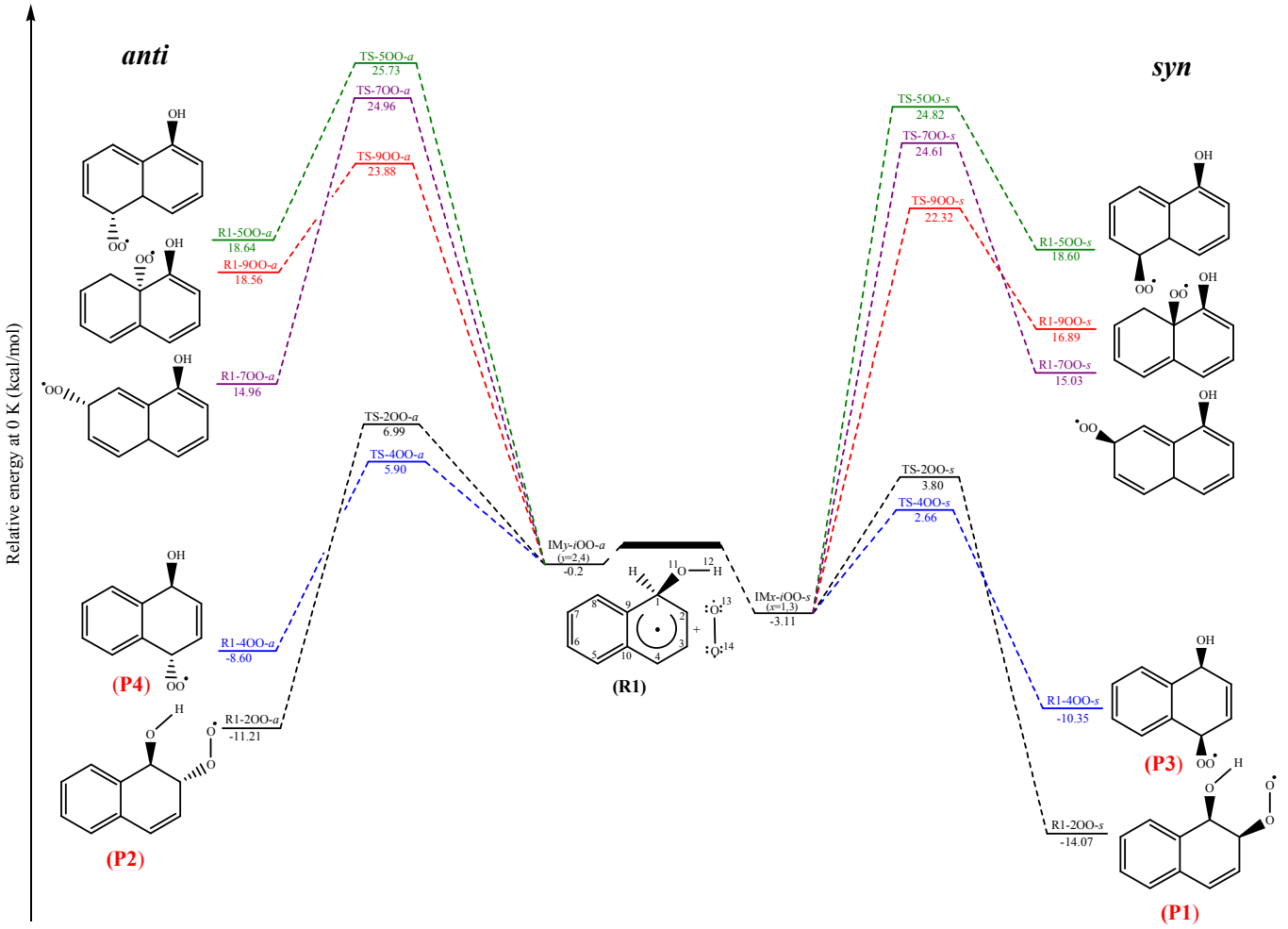

Fig 1. Potential energy diagram for the considered reaction pathways at the UM06-2x/aug-cc-pVTZ level of theory.

2. Computational Details

All calculations that are discussed in the present work have been performed using the Gaussian 09 package of programs[54] at the Flemish Supercomputer Centre. Molecular structures were visualized with Gauss View.[55] The molecular structures and harmonic vibrational frequencies of all stationary points of interest were calculated using Density Functional Theory along with a variety of exchange-correlation functionals, namely the Becke-3-parameters-Lee-Yang-Parr (B3LYP) functional,[46,47] the dispersion corrected ωB97XD exchange-correlation functional,[48] the UM05-2x functional[49] and the UM06-2x functional,[49,50] in conjunction with

Dunning's correlation-consistent basis set of triple-ζ quality augmented with diffuse functions (aug-cc-PVTZ basis set).[51]

Frequency calculations were carried out to check the nature of the identified stationary points. The connections between transition states and the corresponding energy minima have been verified according to intrinsic reaction coordinate (IRC) calculations[56] that were carried out at the B3LYP/6-31G(d,p) level using the second-order Gonzalez-Schlegel integration method.[57,58] In line with these frequency calculations, thermodynamic state functions (*H*, *S*, *G*) were obtained from canonical partition functions obtained for an ideal polyatomic gas under a pressure of 1.0 atm using the standard RRHO (rigid rotor harmonic oscillator) approximation and Boltzmann statistics (see refs 59 and 60 or any textbook of molecular statistical mechanics).

In this study, O_2 addition to the $[C_{10}H_8OH]^\bullet$ complex (R1) is analyzed according to the scheme advocated by Singleton and Cvetanovic.[61] With this scheme, it is assumed that the reaction occurs according to a two-step mechanism, involving first a fast pre-equilibrium between the reactants (R1+O_2) and a pre-reactive complex $[C_{10}H_8OH\ldots O_2]^\bullet$ (IM), followed by the irreversible formation of the naphthalene peroxy radicals $[C_{10}H_8OH\text{-}O_2]^\bullet$ (R2):

$$\text{step 1: } \left[C_{10}H_8OH\right]^\bullet + O_2 \underset{k_{-1}}{\overset{k_1}{\rightleftharpoons}} \left[C_{10}H_8OH...O_2\right]^\bullet$$

$$\text{step 2: } \left[C_{10}H_8OH...O_2\right]^\bullet \xrightarrow{k_2} \text{products}$$

In the above reactions, k_1 is the kinetic rate constant characterizing the forward bimolecular reaction step (in cm^3 $molecule^{-1}$ s^{-1}), whereas k_{-1} and k_2 represent the backward and forward unimolecular reaction rate constants (in s^{-1}). A steady-state analysis of the overall reaction pathway leads to the following expression for the associated rate constant:[61]

$$k_{\text{overall}} = \frac{k_1 k_2}{k_{-1} + k_2} \quad (1)$$

Although the energy barrier for k_{-1} has about the same height as that for k_2, the entropy change for the reverse reaction (IM→R1+O_2) is much larger than for the formation of the products (IM→R2). Thus, k_{-1} is expected to be much larger than k_2 (an assumption that has been checked in details on the basis of RRKM calculations, see data reported in the Supplementary Information). Based on this assumption, the overall rate constant (k_{overall}) can be calculated as follows:

$$k_{overall} = K_c\, k_2 \quad (2)$$

with K_c=k_1/k_{-1} the equilibrium constant for the fast pre-equilibrium between the reactants and the pre-reactive complex (step 1):

$$K_c = \frac{\left[C_{10}H_8OH...O_2\right]^\bullet}{\left[C_{10}H_8OH\right]^\bullet\left[O_2\right]} \quad (3)$$

Considering basic statistical thermodynamic principles (see in particular eq. 26.3-20 in ref. 62), the equilibrium constant of the fast pre-equilibrium between the reactants and the pre-reactive complex can be obtained as:

$$K_c = \frac{Q_{IM}}{Q_{R1}.Q_{O_2}} \times \frac{V_m(T)}{N_{Av}} \times \exp\left[-\frac{\left(E_{IM} - E_{R1} - E_{O_2}\right)}{RT}\right] \quad (4)$$

with N_{Av} the Avogadro number, R the ideal gas constant and $V_m(T)$=RT/P the molar volume of an ideal gas. The kinetic rate constant characterizing the unimolecular dissociation reaction of the pre-reactive complex is obtained in the high pressure limit by means of transition state theory:[35–42]

$$k_2 = \frac{\sigma k_B T}{h} \times \frac{Q_{TS}}{Q_{IM}} \times \exp\left[-\frac{\left(E_{TS} - E_{IM}\right)}{RT}\right] \quad (5)$$

In line with the temperatures at which the experiments by Koch *et al.* were conducted[31–34], kinetic rate constants and branching ratios have been obtained at 298, 336 and 400 K and at a pressure of 1.0 bar (high pressure limit) using transition state theory, and the UM06-2x/aug-cc-pVTZ estimates for activation energies. The rationale behind this choice is that a recent study by Zhao and Truhlar[50] has shown that the UM06-2x exchange-correlation functional is the best one for applications involving main-group thermochemistry, kinetics, noncovalent interactions, and electronic excitation energies to valence and Rydberg states.[50]

For the sake of completeness, it is at last worth reminding that the kinetics of bimolecular and unimolecular reactions in atmospheric chemistry can be determined using conventional transition state theory, along with the following equations:[63–65]

$$k_{TST} = \frac{\sigma k_B T}{h} V_m(T) \frac{Q_{TS}^{\neq}(T)}{Q_A(T).Q_B(T)} \exp\left(-E_a/RT\right) \quad (6)$$

$$k_{TST} = \frac{\sigma k_B T}{h} \frac{Q_{TS}^{\neq}(T)}{Q_A(T)} \exp\left(-E_a/RT\right) \quad (7)$$

In the above equations, σ denotes the reaction symmetry number, Q_A, Q_B, and Q_{TS} represent the total molecular partition functions for the isolated reactants, and transition state associated to the unimolecular dissociation reaction (step 2), respectively. E_a is the classical barrier height (including zero-point vibrational energy contributions), k_B and h are the Boltzmann's and Planck's constants, respectively. Since the computed energy differences account for zero-point vibrational energies, vibrational partition functions were computed using the vibrational ground state as energy reference. Tunneling corrections were assumed to be insignificant, considering the size of the moieties involved in the chemical reactions of interest.

TST gives an estimate of the upper-limit for rate constants as a function of the temperature, and is known to give reliable estimations of rate constants[66,67] in the high pressure limit,[68] especially for cases with significant barrier heights (as is the case here).[69] All supplied rate constants are the results of calculations that were performed using the implementation of this approach in the Kinetic and Statistical Thermodynamical Package (KiSThelP) by Canneaux *et al.*[70] Besides TST, in the present study, statistical RRKM theory[42–44] has been considered to evaluate pressure effects on a microcanonical basis, both in the fall-off regime and towards the high pressure limit, using the implementation of this approach in the KiSThelP program.[70] In these RRKM calculations, a scaling factor of 0.971 was imposed on the frequencies calculated at the UM06-2x/aug-cc-pVTZ level of theory. Collisional stabilization rate constants were computed using Lennard-Jones collision rate theory.[11] The strong collision approximation was used, assuming therefore that every collision deactivates with $\omega = \beta_c.Z_{LJ}.[M]$ being the effective collision frequency, where β_c is the collisional efficiency, Z_{LJ} is the Lennard-Jones collision frequency and [M] is the total gas concentration. The retained value for β_c is 0.2. The collision frequencies (Z_{LJ}) were calculated using the Lennard-Jones parameters: ε/k_B, which depends on the energy depth (ε) of the Lennard-Jones potential, and σ which represents a dimensional scale of the molecular radius.[71] The retained Lennard-Jones potential parameters for pure air as diluent gas amount to σ = 3.522 Å an ε/k_B = 99.2 K.[72,73] For the naphthalene-OH adduct $[C_{10}H_8OH]^\bullet$, the following parameters have been used: σ = 6.57 Å and ε/k_B = 612.7 K.[74]

3. Results and Discussion

3.1. Energetic and thermodynamic parameters

Since the $[C_{10}H_8OH]^\bullet$ (R1) radical has several resonant structures, the addition of triplet molecular ($^3\sum_g$) oxygen to the $[C_{10}H_8OH]^\bullet$ (R1) radical can occur from *syn* and *anti*-directions at five different positions, namely onto the C_2, C_4, C_5, C_7, and C_9-atoms, yielding 10 isomers referred, as in the study by Zhang *et al.*[25] to as the so-called R1-*i*OO-*anti*/*syn* (i = 2, 4, 5, 7, 9) peroxy radicals, respectively (Fig. 1). The B3LYP/6-311+G(2df,p) and BB1K/6-311++G(2df,2p) data obtained by Zhang *et al.*[25] are reported in Table 1, where they can be compared with our newly supplied DFT data. The reader is referred to Table 2 for a presentation at the same theoretical levels of the activation energies to form the peroxy radicals.

In line with chemical intuition, the R1-2OO and R1-4OO *syn*/*anti* radicals are found to be by far the most stable structures, an observation which is easily explained by the fact that with these isomeric structures, aromaticity is preserved in one of the two benzenoid rings, in contrast with the other ones (R1-*i*OO-*syn*/*anti*, with i = 5, 7, and 9) where aromaticity is destroyed in both rings. More specifically, all DFT estimates at room temperature show that O_2 additions onto the C_2 and C_4 positions are exothermic processes ($\Delta H_r < 0$), whereas formation of the R1-*i*OO-*anti*/*syn* (i = 5, 7, 9) peroxy radicals requires much higher reaction enthalpies, ranging from 14.3 to 24.3 kcal mol^{-1} (Table 1). The corresponding energy barriers are also much higher (Table 2, Fig. 1). Hence, the formation of these radicals will be negligible under atmospheric conditions. In the sequel, we shall therefore concentrate on the four lowest chemical pathways, corresponding to O_2 addition processes in *syn* and *anti* modes at the C_2 and C_4 positions. In other words, we shall focus on the formation of the R1-*i*OO-*anti*/*syn* (i= 1, 2) radicals, yielding the **P1**–**P4** products (Figure 1). For the ease of notations, the corresponding chemical pathways will be correspondingly referred to as reaction pathways **1**–**4**, in the section on kinetic parameters.

In sharp contrast with the B3LYP and BB1K results by Zhang *et al.*,[25] all our DFT calculations demonstrate that, among all isomers, the most stable isomer is the R1-2OO-*syn* one. More specifically, in contrast with the B3LYP and BB1K results by Zhang *et al.*[25] (Table 1), the R1-2OO-*syn* isomer is found at all the theoretical levels we considered to be more stable than the R1-2OO-*anti* one. The reactions energies (ΔE_{0K}) characterizing the formation of the R1-2OO-*syn* and R1-4OO-*syn* radicals are all in all lower by about 1.45–2.86 kcal mol^{-1} and 1.75–1.90 kcal mol^{-1} than the reactions energies for the formation of the R1-2OO-*anti* and R1-4OO-*anti* peroxy radicals. These stabilization energies are in line with the energies that are usually associated with classical hydrogen bonds, in the range 1.2 to 7.2 kcal mol^{-1}, and find also their origin into an electrostatic interaction between a positively charged hydrogen atom (H_{12}) and a negatively charged oxygen atom (O_{14}) (see further discussion of structural details). We note that this observation is similar to that made in a recent theoretical study of the atmospheric photo-oxidation mechanisms of toluene,[75] in which the formation of radical structures resulting from the addition of the peroxy and hydroxyl substituents on the same side was found to be energetically more favourable.

Table 1. Reaction energies, reaction enthalpies and Gibb's free reaction energies (in kcal mol^{-1}) for the addition of triplet molecular O_2 on the $[C_{10}H_8OH]^\bullet$ radical.

Species \ Method	B3LYP			ωB97XD			UM05-2x			UM06-2x			literature	
	ΔE_{0K}	$\Delta H°_{298K}$	$\Delta G°_{298K}$	ΔE_{0K}	$\Delta H°_{298K}$	$\Delta G°_{298K}$	ΔE_{0K}	$\Delta H°_{298K}$	$\Delta G°_{298K}$	ΔE_{0K}	$\Delta H°_{298K}$	$\Delta G°_{298K}$	ΔE_{0K}	$\Delta G°_{298K}$
R1 + O_2	0.00	0.00	0.00	0.00	0.00	0.00	0.00	0.00	0.00	0.00	0.00	0.00		
R1-2OO-*syn*	-6.12	-7.05	4.88	-9.67	-10.58	1.23	-11.70	-12.72	-0.57	-14.07	-15.02	-3.08	-6.55[a]	4.49[a]
	(-6.51)	(-7.45)	(4.52)	[-8.86]	[-10.06]	[3.28]							-8.96[b]	2.03[b]
IM-*i*OO-*syn* (*i*=2,4)	-0.11	0.20	8.05	-1.04	-0.77	7.35	-1.96	-1.73	6.64	-3.11	-2.82	5.24		
R1-4OO-*syn*	-2.35	-3.22	8.58	-6.31	-7.28	4.76	-8.13	-9.10	2.96	-10.35	-11.30	0.67	-2.89[a]	8.08[a]
	(-2.84)	(-3.72)	(8.12)	[-5.23]	[-5.78]	[5.56]							-4.59[b]	6.67[b]
R1-5OO-*syn*	23.86	23.42	33.87	22.27	21.73	32.46	21.32	20.76	31.47	18.60	18.05	28.81	21.89[a]	31.96[a]
	(23.43)	(22.97)	(33.48)	[20.04]	[19.34]	[30.50]							23.54[b]	33.82[b]
R1-7OO-*syn*	20.12	19.67	29.51	19.30	18.71	29.40	17.77	17.14	27.82	15.03	14.45	24.99	21.99[a]	31.81[a]
	(19.76)	(19.30)	(29.14)	[17.34]	[16.51]	[28.55]							20.24[b]	30.35[b]
R1-9OO-*syn*	24.81	24.27	35.48	22.10	21.42	32.97	19.68	18.90	30.83	16.89	16.18	27.83	22.83[a]	33.96[a]
	(24.17)	(23.60)	(34.88)	[20.84]	[20.05]	[32.48]							22.90[b]	34.13[b]
R1-2OO-*anti*	-4.67	-5.42	5.82	-7.63	-8.37	2.81	-8.99	-9.87	1.75	-11.21	-12.05	-0.53	-10.35[a]	0.53[a]
	(-4.94)	(-5.69)	(5.56)	[-6.46]	[-7.51]	[4.86]							-9.82[b]	1.03[b]
IM-*i*OO-*anti* (*i*=2,4)	1.89	2.47	8.91	1.33	1.81	8.94	0.76	1.14	8.97	-0.20	0.02	8.84		
R1-4OO-*anti*	-0.58	-1.24	9.85	-4.56	-5.23	5.87	-6.23	-7.02	4.52	-8.60	-9.38	2.15	-2.27[a]	8.65[a]
	(-0.96)	(-1.63)	(9.47)	[-2.67]	[-3.73]	[9.06]							-4.61[b]	6.29[b]
R1-5OO-*anti*	24.36	23.90	34.36	22.50	21.94	32.71	21.49	20.81	32.01	18.64	17.98	29.09	22.20[a]	32.22[a]
	(23.94)	(23.46)	(33.99)	[20.77]	[19.99]	[31.86]							23.11[b]	33.51[b]
R1-7OO-*anti*	20.06	19.62	29.49	19.15	18.60	29.17	17.53	16.95	27.38	14.96	14.34	25.11	19.67[a]	28.94[a]
	(19.73)	(19.28)	(29.01)	[17.51]	[16.64]	[28.94]							20.22[b]	30.38[b]
R1-9OO-*anti*	-	-	-	23.13	22.58	33.65	21.25	20.60	32.16	18.56	17.93	29.39	-	-
				[21.76]	[21.02]	[33.25]								

a: Ref. 25; values obtained at the B3LYP/6-311+G(2df,p) level of theory.
b: Ref. 25; values obtained at the BB1K/6-311++G(2df,2p) level of theory.
- The values in parenthesis were calculated at the B3LYP/6-311+G(2df,p) level of theory (present work).
- The values in square brackets were calculated at the BB1K/6-311++G(2df,2p) level of theory (present work).

It is interesting to note that, although the R1-2OO-*syn* peroxy radical represents the most stable form for O_2 addition to the $[C_{10}H_8OH]^\bullet$ adducts, the corresponding activation energy is slightly larger than for the formation of the R1-4OO-*syn* radical. Also

because of some extra-stabilization due to the formation of an intramolecular hydrogen bond between the terminal oxygen of the peroxy group (O_{14}) and the hydrogen atom of the hydroxyl group (H_{12}), the barrier heights ($\Delta E_{0K}^{\ddagger}$) for O_2 addition from the *syn*-direction are lower than those for the *anti*-direction, by about 1.9 to 3.3 kcal mol^{-1}. Similar observations can be made when Gibb's free activation energies are considered: in spite of slightly unfavourable entropy effects, the Gibb's free energies for the *syn* addition modes in C_2 and C_4 positions (11.95–16.04 and 10.49–14.71 kcal mol^{-1}, respectively) are at all the DFT levels we employed systematically lower than the ones for the *anti* modes (13.42–18.74 and 12.90–17.62 kcal mol^{-1}). Therefore, O_2 addition in *syn* positions will be both thermodynamically and kinetically favoured over O_2 addition in *anti* positions. Among all possible adducts, the formation of the R1-2OO-*syn* isomer will clearly therefore predominate under thermodynamic control, i.e. at chemical equilibrium. Note that kinetic effects may on the contrary favour the formation of the R1-4OO-*syn* isomer (see further). Both for the *syn* and *anti* modes, O_2 addition in C_2 position is thermodynamically favoured over O_2 addition in C_4 position.

Table 2. Activation energies, enthalpies and Gibb's free activation energies (in kcal mol^{-1}) for the addition of triplet molecular O_2 on the $[C_{10}H_8OH]^{\bullet}$ radical.

Method / Species	B3LYP			ωB97XD			UM05-2x			UM06-2x			literature	
	$\Delta E_{0K}^{\ddagger}$	$\Delta H°_{298K}^{\ddagger}$	$\Delta G°_{298K}^{\ddagger}$	$\Delta E_{0K}^{\ddagger}$	$\Delta H°_{298K}^{\ddagger}$	$\Delta G°_{298K}^{\ddagger}$	$\Delta E_{0K}^{\ddagger}$	$\Delta H°_{298K}^{\ddagger}$	$\Delta G°_{298K}^{\ddagger}$	$\Delta E_{0K}^{\ddagger}$	$\Delta H°_{298K}^{\ddagger}$	$\Delta G°_{298K}^{\ddagger}$	$\Delta E_{0K}^{\ddagger}$	$\Delta G°_{298K}^{\ddagger}$
R1 + O_2	0.00	0.00	0.00	0.00	0.00	0.00	0.00	0.00	0.00	0.00	0.00	0.00		
TS-2OO-*syn*	1.29 (3.38)	0.47 (2.62)	11.95 (14.01)	4.97	4.25	15.61	5.06	4.18	16.04	3.80	2.99	14.63	5.19[a] 9.97[b]	15.46[a] 19.98[b]
TS-4OO-*syn*	0.02 (2.29)	-0.72 (1.58)	10.49 (12.79)	3.66	2.99	14.09	3.98	3.19	14.71	2.66	1.90	13.44	2.27[a] 6.79[b]	12.76[a] 17.78[b]
TS-5OO-*syn*	21.08 (23.86)	20.45 (23.31)	31.16 (33.88)	25.79	25.26	35.88	26.40	25.83	36.49	24.82	24.32	34.59	21.63[a] 26.55[b]	32.03[a] 36.97[b]
TS-7OO-*syn*	18.97 (21.64)	18.42 (21.17)	28.31 (30.94)	25.57	25.13	35.11	25.74	25.23	35.45	24.61	24.11	34.35	21.63[a] 27.92[b]	30.93[a] 37.43[b]
TS-9OO-*syn*	20.33 (22.93)	19.35 (22.02)	31.55 (34.10)	24.27	23.44	35.28	23.96	23.13	35.06	22.32	21.54	33.30	22.92[a] 27.32[b]	34.08[a] 38.29[b]
TS-2OO-*anti*	3.21 (5.67)	2.62 (5.13)	13.42 (15.88)	7.70	7.16	17.90	8.25	7.59	18.74	6.99	6.39	17.39	3.99[a] 9.92[b]	14.15[a] 20.12[b]
TS-4OO-*anti*	2.86 (5.22)	2.32 (4.75)	12.90 (15.22)	6.99	6.57	16.80	7.31	6.69	17.62	5.90	5.31	16.23	3.63[a] 7.86[b]	13.79[a] 18.5[b]
TS-5OO-*anti*	20.96 (23.81)	20.44 (23.36)	30.48 (33.35)	26.37	25.97	35.82	26.99	26.50	36.84	25.73	25.30	35.33	21.96[a] 26.89[b]	32.36[a] 37.09[b]
TS-7OO-*anti*	19.13 (21.83)	18.56 (21.38)	28.65 (30.99)	25.74	25.37	34.72	26.03	25.51	35.80	24.96	24.44	34.82	21.82[a] 28.3[b]	30.98[a] 37.57[b]
TS-9OO-*anti*	22.37 (25.01)	21.65 (24.35)	33.11 (35.70)	25.69	25.14	36.16	25.61	24.98	36.31	23.88	23.32	34.48	25.0[a] 28.9[b]	35.68[a] 39.7[b]

a: Ref. 25; values obtained at the B3LYP/6-311+G(2df,p) level of theory.
b: Ref. 25; values obtained at the BB1K/6-311++G(2df,2p) level of theory.
- The values in parenthesis were calculated at the B3LYP/6-311+G(2df,p) level of theory (present work).

We note that the different exchange-correlation functionals that have been employed predict large differences in the relative energies of the identified stationary points, especially with regards to the extent of activation energies. As was to be expected, due to a large self-interaction error, the B3LYP functional systematically yields strong underestimations of the computed activation energies, of the order of 3–4 kcal mol^{-1}, compared with the results obtained with the *ω*B97XD, UM05-2x and UM06-2x functionals, which most generally do not differ by more than 2 kcal mol^{-1}. Interestingly, we find that the UM06-2x/aug-cc-pVTZ activation energies systematically underestimate the ωB97XD/aug-cc-pVTZ ones by 1 to 2 kcal mol^{-1}, which in turn slightly underestimate the UM05-2x/ aug-cc-pVTZ energy barriers, within 0 to 1 kcal mol^{-1}. Therefore, if rather large differences are to be expected with the correspondingly obtained kinetic rate constants, the ultimately obtained branching ratios will exhibit a rather limited dependence upon the employed exchange-correlation functionals.

At last, we note that our B3LYP/aug-cc-pVTZ results for reaction energies and activation energies exhibit considerable differences, up to 3 kcal mol^{-1}, compared with the B3LYP/6-311+G(2df,p) results obtained by Zhang *et al.* in ref. 25. These differences, most obviously, reflect the greater size, flexibility and quality of the aug-cc-pVTZ basis set, which incorporates on total 805 atomic functions, compared with a total of 496 atomic functions for the 6-311+G(2df,p) basis set. Besides, it is worth reminding that the 6-311G basis set from which the 6-311+G(2df,p) derives is known to exhibit a too compact 2*p* space,[76] and to be effectively a basis set of double-zeta quality only in the *s*-space, due to improperly balanced expansion coefficients.[77]

3.2. Structural characteristics of stationary points

The optimized geometries of all identified stationary points involved in the chemical pathways for O_2 addition onto the C_2 and C_4 atoms of the $[C_{10}H_8\text{-}OH]^{\bullet}$ energized adduct are supplied at all selected DFT levels in Tables 3 and 4, respectively. The reader is correspondingly referred to Figure 2 for detailed atom labelling. Upon examining this Figure, it is clear that, in contrast with the R1-2OO-*syn* and R1-4OO-*syn* peroxy radical species, the structures describing the R1-2OO-*anti* and R1-4OO-*anti* isomers do not allow the formation of an intramolecular hydrogen bond between the hydroxyl (OH) and peroxy (O_2) substituents. Whatever the employed exchange-correlation functional, NBO calculations deliver charges around +0.48 and –0.20 for H_{12} and O_{14}, respectively. These atoms exhibit inter-distances in the range 1.97–2.03 Å and 2.27–2.33 Å for the R1-2OO-*syn* and R1-4OO-*syn* radicals, respectively, which are compatible with the idea of an hydrogen bond. On the other hand,

these interdistances increase to ~3.87 and ~5.04 Å within the R1-2OO-*anti* and R1-4OO-*anti* structures, and become clearly far too large for any significant stabilizing electrostatic interactions. These structural preferences explain the slightly larger stability, by 1.45–2.86 to 1.75–1.9 kcal mol^{-1}, of the R1-2OO-*syn* and R1-4OO-*syn* structures, relative to the *anti* ones.

Addition of O_2 onto the C_2 atom within the R1 energized adduct results into a lengthening of the C_1–C_2 and C_2–C_3 bonds next to the site of addition, by ~0.03 Å and ~0.13 Å, respectively (Table 3). This increase in bond lengths obviously reflects the formation of single C–C bonds around the site of the addition, along with transfer of the π bond electron density to the newly formed C_2–O_{13} bond. Similar structural variations are observed for O_2 addition in C_4 position (Table 4), namely an increase of the C_3–C_4 and C_4–C_{10} bond lengths by 0.07–0.09 Å.

In addition, in comparison with the geometries obtained for the $[C_{10}H_8OH]^{\bullet}$ adduct (R1) (Tables 3 and 4), addition of O_2 to the R1 radical results in a shortening of the C_1–O_{11} bond. For the R1-2OO-*syn* radical, in which the intramolecular hydrogen binding is energetically stronger, the length of the C_1–O_{11} bond is reduced by ~0.03 Å. This reduction in length is a significantly more important structural variation than that observed with the R1-4OO-*syn* radical, in which the C_1–O_{11} bond length is reduced by only 0.01 Å, and is therefore consistent with the idea of a stronger intramolecular hydrogen bond. Also in line with the formation of an intramolecular hydrogen bond, the O_{13}–O_{14} bond length increases from 1.19–1.21 Å to 1.29–1.32 Å, when the molecular structure evolves from the R1 energized adduct to the R1-2OO-*syn* and R1-4OO-*syn* peroxy radicals.

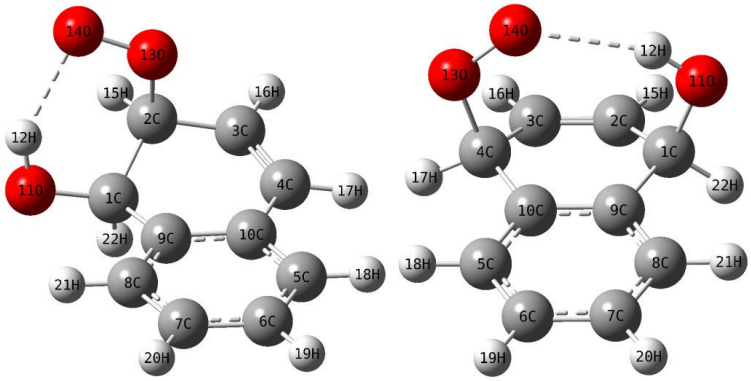

R1-2OO-*syn* peroxy radical R1-4OO-*syn* peroxy radical

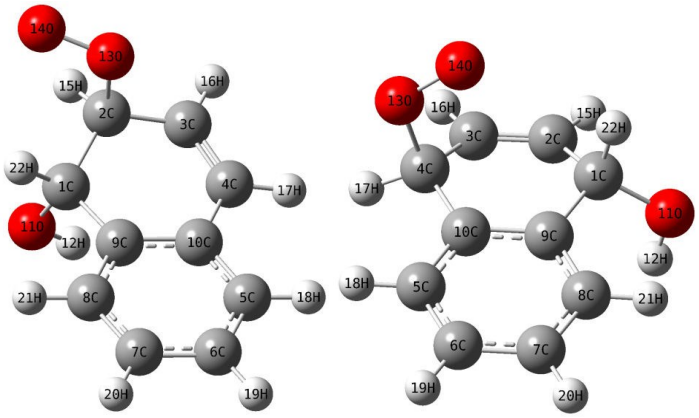

R1-2OO-*anti* peroxy radical R1-4OO-*anti* peroxy radical

Fig 2. Optimized geometries of the R1-2OO and R1-4OO peroxy radicals.

In analogy with the study by Huang *et al.* of hydroxyxcyclohexadienyl peroxy radicals,[78] the transition states for O_2 addition at the C_2 and C_4-positions in the R1 energized adduct involve a six-membered cyclic structure [C_1–O_{11}–H_{12}–O_{14}–O_{13}–C_i (i= 2, 4)] in which the O_{14}, O_{13} and C_i (i= 2, 4) atoms are not co-linear. Indeed, the corresponding bond angles are around 112° (Tables 3 and 4). Like the corresponding energy minima (Figure 2), these transition state structures are also stabilized by an intramolecular hydrogen bond (H_{12}–O_{14}). The hydrogen bond lengths within the TS-2OO-*syn* and TS-4OO-*syn* structures amount to 3.18–3.20 Å and 2.28–2.30 Å, respectively. It can also be noticed that in the transition states involved in the formation of the R1-2OO-*syn* and R1-4OO-*syn* radical species, the forming C_2–O_{13} and C_4–O_{13} bond lengths are significantly much longer than in the related products, by 69.09–70.43 % and 70.85–72.27 %, respectively.

For the sake of completeness and clarity, it is worth noticing that intermediates IM1 and IM3 on pathways **1** and **3** (O_2 additions in *syn* mode in C_2 or C_4 positions) are structurally almost the same and exhibit practically equal energies, which cannot be distinguished on the scale of Figure 1. Similarly, IM2 and IM4 on pathways **2** and **4** (O_2 additions in *anti* mode in C_2 or C_4 positions) have almost the same structures, with almost equal energies.

Table 3. Structural parameters for all the stationary points that are involved in the reaction R1+O_2⇌R1-2OO-*syn* pathway (see Fig. 2 for detailed atom labelling).

Parameter \ Method	B3LYP				ωB97XD				UM05-2x				UM06-2x			
	R	IM	TS	P	R	IM	TS	P	R	IM	TS	P	R	IM	TS	P
r (C_1–C_2)	1.495	1.495	1.498	1.530	1.494	1.494	1.497	1.526	1.491	1.492	1.494	1.519	1.494	1.495	1.497	1.525
r (C_2–C_3)	1.367	1.365	1.396	1.495	1.363	1.361	1.399	1.496	1.363	1.362	1.399	1.495	1.363	1.362	1.399	1.499
r (C_3–C_4)	1.401	1.401	1.368	1.338	1.398	1.398	1.361	1.332	1.397	1.397	1.360	1.331	1.400	1.399	1.362	1.333
r (C_4–C_{10})	1.429	1.429	1.443	1.459	1.430	1.431	1.448	1.463	1.429	1.430	1.447	1.461	1.431	1.432	1.449	1.464
r (C_1–C_9)	1.517	1.516	1.519	1.518	1.514	1.514	1.516	1.514	1.509	1.510	1.511	1.510	1.513	1.514	1.515	1.513
r (C_9–C_{10})	1.415	1.414	1.409	1.407	1.407	1.406	1.402	1.400	1.404	1.404	1.400	1.398	1.408	1.407	1.402	1.401
r (C_1–O_{11})	1.448	1.442	1.423	1.411	1.431	1.424	1.410	1.400	1.436	1.431	1.416	1.406	1.429	1.424	1.412	1.402
r (C_2–O_{13})	-	3.403	2.164	1.495	-	3.198	2.115	1.473	-	3.274	2.090	1.472	-	3.131	2.109	1.467
r (H_{12}–O_{14})	-	3.379	3.201	1.971	-	3.440	3.201	1.985	-	3.421	3.180	2.017	-	3.459	3.178	2.033
r (O_{13}–O_{14})	1.206	1.213	1.245	1.317	1.196	1.201	1.231	1.301	1.187	1.188	1.223	1.297	1.190	1.192	1.224	1.298
θ(C_1–O_{11}–H_{12})	107.72	107.36	107.56	108.76	107.57	107.24	107.59	108.54	107.58	107.39	107.64	109.10	107.68	107.56	107.68	109.21
θ(C_2–O_{13}–O_{14})	-	94.48	111.92	112.47	-	97.30	112.20	112.55	-	98.44	112.06	111.92	-	100.46	111.86	112.29

- Bond lengths are in angstrom (Å) unit and torsion and dihedral angles are in degrees (°)

Table 4. Structural parameters for all the stationary points that are involved in the reaction R1+O_2⇌R1-4OO-*syn* pathway (see Fig. 2 for detailed atom labelling).

Parameter \ Method	B3LYP				ωB97XD				UM05-2x				UM06-2x			
	R	IM	TS	P	R	IM	TS	P	R	IM	TS	P	R	IM	TS	P
r (C_1–C_2)	1.495	1.495	1.497	1.503	1.494	1.494	1.496	1.503	1.491	1.492	1.494	1.500	1.494	1.495	1.497	1.504
r (C_2–C_3)	1.367	1.365	1.348	1.328	1.363	1.361	1.343	1.323	1.363	1.362	1.342	1.322	1.363	1.362	1.344	1.324
r (C_3–C_4)	1.401	1.401	1.421	1.487	1.398	1.398	1.421	1.490	1.397	1.397	1.422	1.489	1.400	1.399	1.423	1.493
r (C_4–C_{10})	1.429	1.429	1.439	1.495	1.430	1.431	1.442	1.497	1.429	1.430	1.441	1.494	1.431	1.432	1.442	1.498
r (C_1–C_9)	1.517	1.516	1.514	1.513	1.514	1.514	1.511	1.511	1.509	1.510	1.507	1.506	1.513	1.514	1.510	1.510
r (C_9–C_{10})	1.415	1.414	1.407	1.396	1.407	1.406	1.399	1.390	1.404	1.404	1.396	1.387	1.408	1.407	1.400	1.390
r (C_1–O_{11})	1.448	1.443	1.437	1.437	1.431	1.424	1.421	1.422	1.436	1.431	1.427	1.428	1.429	1.424	1.421	1.422
r (C_4–O_{13})	-	2.961	2.148	1.536	-	2.841	2.103	1.490	-	2.966	2.070	1.496	-	2.909	2.094	1.490
r (H_{12}–O_{14})	-	2.460	2.290	2.318	-	2.457	2.300	2.268	-	2.416	2.285	2.328	-	2.399	2.281	2.271
r (O_{13}–O_{14})	1.206	1.213	1.243	1.305	1.196	1.201	1.229	1.293	1.187	1.188	1.222	1.290	1.190	1.192	1.222	1.290
θ(C_1–O_{11}–H_{12})	107.72	107.36	106.46	106.62	107.57	107.24	106.39	106.43	107.58	107.39	106.36	106.45	107.68	107.56	106.57	106.62
θ(C_4–O_{13}–O_{14})	-	105.04	111.87	113.48	-	103.25	111.14	113.20	-	101.06	110.22	112.22	-	99.08	109.88	112.61

- Bond lengths are in angstrom (Å) unit and torsion and dihedral angles are in degrees (°)

Hammond's postulate states that the structure of a transition state resembles that of the species nearest to it in free energy. This principle is usually quantified in terms of the position of the transition structure along the reaction coordinate, n_T, as defined by Agmon:[79]

$$n_T = \frac{1}{2-(\Delta G / \Delta G^{\neq})} \quad (8)$$

The magnitudes of n_T, indicates the degree of similarity between the transition structure and the product. According to the above equation, the position of the transition state along the reaction coordinate is determined solely by the Gibb's free reaction energy, ΔG, and the Gibb's free activation energy, $\Delta G^{\neq}$. DFT estimates of n_T values for the *syn*-addition of O_2 to the $[C_{10}H_8OH]^{\bullet}$ radical are supplied in Table 5. In line with the previously obtained energy profiles (Figure 1), and the structural observations made in the preceding section, the obtained values imply that, at all considered levels of theory, the transition state involved in the formation of the R1-4OO-*syn* radical is more similar to the product than the transition state involved in the formation of the R1-2OO-*syn* radical. The same observation can be made when considering the *anti* mode for O_2 addition onto the $[C_{10}H_8OH]^{\bullet}$ radical.

Table 5. Analysis of the chemical pathways of interest in terms of n_T values.

Pathway \ Method	B3LYP	ωB97XD	UM05-2x	UM06-2x
R1+O_2 ⇌ R1-2OO-*syn*	0.6282	0.5205	0.4913	0.4524
R1+O_2 ⇌ R1-4OO-*syn*	0.8460	0.6016	0.5560	0.5128
R1+O_2 ⇌ R1-2OO-*anti*	0.6383	0.5426	0.5245	0.4925
R1+O_2 ⇌ R1-4OO-*anti*	0.8086	0.6058	0.5736	0.5355

3.3. Natural bond orbital analysis

Delocalization of electron density among the filled (bonding or lone pair) Lewis type NBOs and the empty (antibonding and Rydberg) non-Lewis NBOs leads to transfer of occupancy from the localized NBOs of the idealized Lewis structure into the empty non-Lewis orbitals, resulting into a significant departure from an idealized Lewis structure description. This transfer is referred to as a "delocalization" correction to the zero-order natural Lewis structure through a stabilizing donor-acceptor interaction. The energies of these interactions can be estimated by means of second-order perturbation theory.[53] For each donor NBO(i) and acceptor NBO(j), the stabilization energy (E_2) associated with the $i \rightarrow j$ delocalization can be estimated as follows:[80]

$$E_2 = \Delta E_{ij} = q_i \left[\frac{F^2_{(i,j)}}{\varepsilon_i - \varepsilon_j} \right] \quad (9)$$

where q_i is the donor orbital occupancy, ε_i and ε_j are diagonal elements (orbital energies) of the NBO Fock matrix, and $F_{(i,j)}$ are off-diagonal elements of this matrix.

In line with the formation of intramolecular hydrogen bonds between the hydroxyl and peroxy substituents, more specifically between H_{12} and O_{14}, the NBO analysis of donor-acceptor interactions (Table 6) shows that, for both the R1-2OO-*syn* and R1-4OO-*syn* isomers, rather significant stabilization energies (E_2) are associated with electron delocalization from the non-bonding lone-pair orbital in the peroxy substituent [$n(O_{14})$] to the $\sigma^*_{O11-H12}$ antibonding orbital in the hydroxyl substituent. As was noted for the hydroxycyclohexadienyl peroxy radical,[76] hyperconjugative interactions lead also to an increase in the population of the $\sigma^*_{O11-H12}$ antibonding orbital, which weakens in turn the O_{11}–H_{12} bond.

Table 6. NBO occupancies and delocalization energies (E_2) (in kcal mol^{-1}) characterizing at different DFT levels the R1-2OO-*syn* (**1**) and R1-4OO-*syn* (**2**) peroxy radicals (results obtained using the aug-cc-pVTZ basis set).

	B3LYP		*ω*B97XD		UM05-2x		UM06-2x	
	(**1**)	(**2**)	(**1**)	(**2**)	(**1**)	(**2**)	(**1**)	(**2**)
Occupancies								
$\sigma(O_{11}–H_{12})$	0.9943	0.9945	0.9943	0.9944	0.9946	0.9948	0.9943	0.9945
$\sigma^*(O_{11}–H_{12})$	0.0111	0.0065	0.0101	0.0063	0.0083	0.0053	0.0080	0.0058
$n_1(O_{14})$	0.9927	0.9970	0.9932	0.9968	0.9936	0.9969	0.9937	0.9967
$n_2(O_{14})$	0.9810	0.9749	0.9826	0.9789	0.9849	0.9811	0.9853	0.9812
Delocalization energies (E_2)								
$n_1(O_{14})\rightarrow\sigma^*(O_{11}–H_{12})$	1.43	< 0.25	1.55	0.38	1.53	< 0.25	1.45	< 0.25
$n_2(O_{14})\rightarrow\sigma^*(O_{11}–H_{12})$	1.74	0.37	1.97	0.53	1.05	0.31	0.79	0.35

More specifically, the NBO results indicate an hyperconjugative $n_1(O_{14})\rightarrow\sigma^*_{O11–H12}$ interaction energy in the range 0.79–1.97 kcal mol^{-1} for the R1-4OO-*syn* isomer. For the R1-2OO-*syn* isomer, delocalization of the oxygen lone pairs, n_1 and n_2, of the O_{14} atom onto the H_{12} atom results in net stabilizations in the energy range 1.43–1.55 kcal mol^{-1}. Hyperconjugative $n_1(O_{14})\rightarrow\sigma^*_{O11–H12}$ and $n_2(O_{14})\rightarrow\sigma^*_{O11–H12}$ interactions for the R1-4OO-*syn* radical are lower than 0.38 and 0.53 kcal mol^{-1}, respectively. Besides, decrease of the extent of delocalization of the $n(O_{14})$ lone pair onto the $\sigma^*_{O11–H12}$ antibonding orbital from the R1-2OO-*syn* to the R1-4OO-*syn* structures is concomitant with an increase of the occupation of one of the non-bonding lone-pair orbitals on the O_{14} atom, more specifically $n_1(O_{14})$, and a decrease of the population of the other lone pair, $n_2(O_{14})$.

The electron density in the $\sigma^*(O_{11}–H_{12})$ antibonding orbital in the R1-2OO-*syn* peroxy radical is larger than that found for the R1-4OO-*syn* peroxy radical. Therefore, and also in line with the formation of a stronger intramolecular $H_{12}–O_{14}$ hydrogen bond in the R1-2OO-*syn* structure, the $O_{11}–H_{12}$ hydroxyl bond in the R1-2OO-*syn* isomer is weaker than the $O_{11}–H_{12}$ hydroxyl bond in the R1-4OO-*syn* isomer.

3.4. Kinetic parameters

All kinetic rate constants that are supplied in the sequel were obtained according to our best estimates of energy barriers, i.e. using DFT along with the UM06-2x exchange-correlation functional. Effective rate constants have been computed upon the assumption of a two-step mechanism, involving first a fast and reversible pre-equilibrium between the reactants (R1 and O_2) and a pre-reactive complex $[C_{10}H_8OH…O_2]^\bullet$ (IM), followed by the irreversible formation of the naphthalene peroxy radicals R1-*i*OO-*syn*/*anti* (*i*=2,4):

$$\text{step1: } \left[C_{10}H_8OH\right]^\bullet + O_2 \underset{k_{-1}}{\overset{k_1}{\rightleftharpoons}} \left[C_{10}H_8OH...O_2\right]^\bullet$$

$$\text{step2: } \left[C_{10}H_8OH...O_2\right]^\bullet \xrightarrow{k_2} \left[C_{10}H_8OH-O_2\right]^\bullet$$

A steady-state analysis upon the above sequence of reactions leads to the following expressions for the effective rate constants characterizing the four retained chemical pathways:

$$k_{eff}(\mathbf{1}) = \frac{k_{(R1+O_2\rightarrow IM1)}\, k_{(IM1\rightarrow R1\text{-}2OO\text{-}syn)}}{k_{(IM1\rightarrow R1+O_2)} + k_{(IM1\rightarrow R1\text{-}2OO\text{-}syn)}} \quad (10)$$

$$k_{eff}(\mathbf{2}) = \frac{k_{(R1+O_2\rightarrow IM2)}\, k_{(IM2\rightarrow R1\text{-}2OO\text{-}anti)}}{k_{(IM2\rightarrow R1+O_2)} + k_{(IM2\rightarrow R1\text{-}2OO\text{-}anti)}} \quad (11)$$

$$k_{eff}(\mathbf{3}) = \frac{k_{(R1+O_2\rightarrow IM3)}\, k_{(IM3\rightarrow R1\text{-}4OO\text{-}syn)}}{k_{(IM3\rightarrow R1+O_2)} + k_{(IM3\rightarrow R1\text{-}4OO\text{-}syn)}} \quad (12)$$

$$k_{eff}(\mathbf{4}) = \frac{k_{(R1+O_2\rightarrow IM4)}\, k_{(IM4\rightarrow R1\text{-}4OO\text{-}anti)}}{k_{(IM4\rightarrow R1+O_2)} + k_{(IM4\rightarrow R1\text{-}4OO\text{-}anti)}} \quad (13)$$

with **1** and **2** denoting the formation of the R1-2OO-*syn/anti* radicals, and **3** and **4** denoting the formation of the R1-4OO-*syn/anti* radicals, respectively. In the above equations, $k_{(R1+O2\rightarrow IMi,\ i=1\text{-}4)}$ is the kinetic rate constant characterizing the forward bimolecular reaction step (in cm^3 molecule^{-1} s^{-1}), whereas $k_{(IMi\rightarrow R1\text{-}i OO(i=2,4)\text{-}syn/anti)}$ and $k_{(IMi\rightarrow R1+O2,\ i=1–4)}$ represent the forward and backward unimolecular reaction rate constants (in s^{-1}).

Whatever the considered temperature, the effective rate constant for the formation of the R1-4OO-*syn* radical is larger than that obtained for the R1-2OO-*syn* radical, which is in line with a reduction of the activation energy barrier, by ~1.1 kcal mol^{-1} (UM06-2x/aug-cc-pVTZ estimate), on the corresponding chemical reaction pathways. Indeed, the supplied TST and RRKM results (Tables 7 and 8) obtained along with the UM06-2x/aug-cc-pVTZ approach indicate that rate constants [k_2(**3**)] for the [IM3→R1-4OO-*syn*] unimolecular rearrangement reaction step are larger by factors ranging from 4 to 6, than the rate constants [k_2(**1**)] obtained for the [IM1→R1-2OO-*syn*] unimolecular reaction step. At a pressure of 1.0 bar, the formation of the R1-4OO-*syn* species will therefore clearly predominate over the formation of the R1-2OO-*syn* species. The same observation holds for pressures ranging from 10^{-12} to 10^4 bars (see Tables S1a–S1f in the Supplementary Information). As is to be expected, because of the involved positive energy barriers, these rate constants increase gradually with increasing temperatures. Rather unsurprisingly, since the equilibrium constants for the first reversible reaction step ($K_c = K_p/RT$) do not depend very much on the site of addition (see data supplied in Tables S2a–S2i in the Supplementary Information), this results in turn into a larger effective rate constant, by about one order of magnitude, for addition of O_2 in *syn* mode and in C_4 position, compared with the effective rate constants obtained for O_2 addition in *syn* mode and in C_2 position.

Similar observations can be made for the *anti* modes of addition. Here also, in line with lower activation energies (by ~1.1 kcal mol^{-1} as well), rate constants [k_2(**4**)] for the [IM4→R1-4OO-*anti*] unimolecular rearrangement reaction step are larger by factors ranging from 4 to 7, than the rate constants [k_2(**2**)] obtained for the [IM2→R1-2OO-*anti*] unimolecular reaction step. At a pressure of 1.0 bar, the formation of the R1-4OO-*anti* species will therefore also clearly predominate over the formation of the R1-2OO-*anti* species. The same observation holds for pressures ranging from 10^{-12} to 10^4 bars (see Tables S1a–S1f in the Supplementary Information). Again, since the equilibrium constants for the first reversible reaction do not depend very much on the site of addition (see data supplied in Tables S2a–S2i in the Supplementary Information), this results in turn into a larger effective rate constant, by about one order of magnitude, for addition of O_2 in *anti* mode and in C_4 position, compared with the effective rate constants obtained for O_2 addition in *anti* mode and in C_2 position. Thus, whatever the addition (*syn* or *anti*) mode, O_2 addition in C_4 position is kinetically favoured over O_2 addition in C_2 position, in contrast with the expectations drawn from thermodynamics and reaction energies.

Since the involved energy barriers are significantly larger, by ~3.20 kcal mol^{-1}, the formation of the R1-2OO-*anti* and R1-4OO-*anti* species is characterized by significantly lower rate constants at the considered temperatures (298, 336, and 400 K), by one to two orders of magnitude, compared with the formation of the R1-2OO-

syn and R1-4OO-*syn* isomers (Tables 7 and 8). With one to two orders of magnitude only of discrepancy, our theoretical effective kinetic rate constants [k_{eff}(**3**)] for the fastest chemical reaction pathway (O_2 addition in *syn* mode and in C_4 position) appear to be in excellent agreement with the available experimental data reported at 298, 336 and 400 K by Koch *et al.*[22,31–33] an observation which validates the proposed two-step mechanism.

Table 7. Unimolecular rate constants (in s^{-1}), and effective rate constants (in cm^3 $molecule^{-1}$ s^{-1}) for the reported reaction channels obtained by means of TST theory (P = 1 bar), according to the computed UM06-2x/aug-cc-pVTZ energy barrier (x=1 or 3, y=2 or 4).

T (K)	Rate constant						Effective rate constant (cm^3 $molecule^{-1}$ s^{-1})				k_{exp} [31-34]
	anti mode			*syn* mode			*anti* mode		*syn* mode		
	IMx→R1+O_2 (k_{-1})	IM2→R1-2OO k_2(**2**)	IM4→R1-4OO k_2(**4**)	IMy→R1+O_2 (k_{-1})	IM1→R1-2OO k_2(**1**)	IM3→R1-4OO k_2(**3**)	R1+O_2⇌R1-2OO [k_{eff}(**2**)]	R1+O_2⇌R1-4OO [k_{eff}(**4**)]	R1+O_2⇌R1-2OO [k_{eff}(**1**)]	R1+O_2⇌R1-4OO [k_{eff}(**3**)]	
298	1.88×10^{19}	1.16×10^{6}	9.12×10^{6}	4.36×10^{16}	1.73×10^{5}	1.05×10^{6}	4.82×10^{-21}	3.79×10^{-20}	3.83×10^{-19}	2.32×10^{-18}	$(8.0\pm3.0)\times10^{-16}$
336	3.92×10^{18}	4.92×10^{6}	3.10×10^{7}	1.80×10^{16}	6.95×10^{5}	3.49×10^{6}	2.41×10^{-20}	1.52×10^{-19}	1.05×10^{-18}	5.23×10^{-18}	$(0.8\pm0.3)\times10^{-16}$
400	5.61×10^{17}	2.98×10^{7}	1.43×10^{8}	6.11×10^{15}	3.93×10^{6}	1.56×10^{7}	1.85×10^{-19}	8.89×10^{-19}	3.65×10^{-18}	1.43×10^{-17}	1.1×10^{-16}

Table 8. Unimolecular rate constants (in s^{-1}), and effective rate constants (in cm^3 $molecule^{-1}$ s^{-1}) for the reported reaction channels obtained by means of RRKM theory (P = 1 bar), according to the computed UM06-2x/aug-cc-pVTZ energy barrier (x=1 or 3, y=2 or 4).

T (K)	Rate constant						Effective rate constant (cm^3 $molecule^{-1}$ s^{-1})				k_{exp} [31-34]
	anti mode			*syn* mode			*anti* mode		*syn* mode		
	IMx→R1+O_2 (k_{-1})	IM2→R1-2OO k_2(**2**)	IM4→R1-4OO k_2(**4**)	IMy→R1+O_2 (k_{-1})	IM1→R1-2OO k_2(**1**)	IM3→R1-4OO k_2(**3**)	R1+O_2⇌R1-2OO [k_{eff}(**2**)]	R1+O_2⇌R1-4OO [k_{eff}(**4**)]	R1+O_2⇌R1-2OO [k_{eff}(**1**)]	R1+O_2⇌R1-4OO [k_{eff}(**3**)]	
298	1.88×10^{19}	1.17×10^{6}	8.92×10^{6}	4.36×10^{16}	1.77×10^{5}	1.07×10^{6}	4.85×10^{-21}	3.71×10^{-20}	3.92×10^{-19}	2.36×10^{-18}	$(8.0\pm3.0)\times10^{-16}$
336	3.92×10^{18}	4.85×10^{6}	2.90×10^{7}	1.80×10^{16}	7.08×10^{5}	3.53×10^{6}	2.68×10^{-20}	1.60×10^{-19}	1.18×10^{-18}	5.90×10^{-18}	$(0.8\pm0.3)\times10^{-16}$
400	5.61×10^{17}	2.77×10^{7}	1.17×10^{8}	6.11×10^{15}	3.96×10^{6}	1.55×10^{7}	2.31×10^{-19}	9.79×10^{-19}	4.90×10^{-18}	1.91×10^{-17}	1.1×10^{-16}

The reader is referred to Figure 3 for an Arrhenius plot of the obtained RRKM estimates at a pressure of 1 bar of the effective rate constants for O_2 addition in C_2 and C_4 positions and in the *syn*/*anti* addition modes (pathways **1**–**4**), according to the UM06-2x/aug-cc-pVTZ estimates of energy barriers. This Figure clearly confirms that the production of the R1-4OO-*syn* peroxy radical dominates the overall reaction mechanism under atmospheric pressure and at temperatures ranging from 298 to 400 K. The same conclusion holds at much lower pressures, down to 10^{-12} bar (see Tables S2a–S2i of the Supplementary Information).

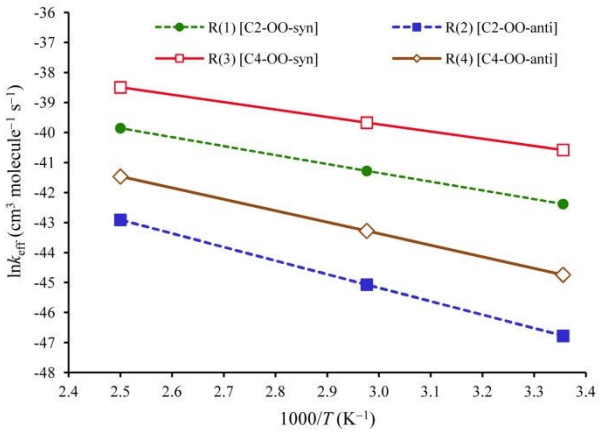

Fig 3. Arrhenius plot of the obtained RRKM bimolecular rate constants (for R1+O_2⇌R1-*i*OO-*syn*, with i=2,4) using the UM06-2x/aug-cc-pVTZ approach. Legend: (●) theoretical rate constant obtained for the R1+O_2⇌R1-2OO-*syn* pathway; (■) theoretical rate constant obtained for the R1+O_2⇌R1-2OO-*anti* pathway; (□) theoretical rate constant obtained for the R1+O_2⇌R1-4OO-*syn* pathway; (◇) theoretical rate constant obtained for the R1+O_2⇌R1-4OO-*anti* pathway.

For the sake of more quantitative insights into the regioselectivity of O_2 addition on the $[C_{10}H_8OH]^{\bullet}$ radical, we report in Table 9 branching ratios at P =1.0 bar and temperatures of 298, 336, and 400 K, which were obtained for the four retained chemical pathways according to the TST and RRKM estimates for effective rate constants (equations 10–13). Under these conditions, TST and RRKM estimates of branching ratios are almost identical.

$$R(i) = \frac{k_{eff}(i)}{k_{eff}(1) + k_{eff}(2) + k_{eff}(3) + k_{eff}(4)}; \quad i = 1,2,3,4 \qquad (14)$$

Further RRKM estimates of these branching ratios at the same temperatures and at pressures ranging from 10^{-12} to 10^{4} bars are supplied in Tables S2a–S2i of the Supplementary Information.

Table 9. Branching ratios for the reported reaction channels obtained by means of TST and RRKM theories (P =1 bar), according to the computed UM06-2x/aug-cc-pVTZ energy barriers.

Pathway \ Theory	TST			RRKM		
	298 K	336 K	400 K	298 K	336 K	400 K
R1+O_2 ⇌ R1-2OO-*syn*	13.95	16.26	19.19	14.06	16.29	19.36
R1+O_2 ⇌ R1-2OO-*anti*	0.18	0.37	0.97	0.17	0.37	0.91
R1+O_2 ⇌ R1-4OO-*syn*	84.50	81.01	75.17	84.44	81.14	75.86
R1+O_2 ⇌ R1-4OO-*anti*	1.38	2.35	4.67	1.33	2.20	3.87

In Figures 4 and 5, we display the evolution of branching ratios for the *syn*-addition of O_2 in C_2 and C_4 positions as a function of the temperature and pressure, respectively (see also Table 8 and Table S3a–S3f of the Supplementary Information for the corresponding numerical values). These data show that the regioselectivity of the reactions slightly decreases with increasing temperatures (Figure 4) and decreasing pressures (Figure 5). In line with the computed energy profile and kinetic rate constants, the formation of the R1-4OO-*syn* isomer (pathway **3**) clearly predominates over the formation of the R1-2OO-*syn* isomer (pathway **1**). In view of the supplied RRKM data (see Tables S2a–S2i of the Supplementary Information), it is more than certain that, at different temperatures, the production of the R1-4OO-*syn* species dominates the overall reaction mechanism, and this down to extremely low pressures, larger than 10^{-12} bar. Note nevertheless that the computed regioselectivity indices become almost equal to zero at 400 K and pressures lower than 10^{-6} bar. At such pressures and temperatures, the reaction is therefore no longer regioselective, and these both for the *syn* and *anti* modes of addition.

Table 10. Branching ratios for the reported reaction channels obtained by means of RRKM theory (P=1 bar), at different DFT levels.

Pathway \ Theory	B3LYP/aug-cc-pVTZ			ωB97XD/aug-cc-pVTZ			UM05-2x/aug-cc-pVTZ			UM06-2x/aug-cc-pVTZ		
	298 K	336 K	400 K	298 K	336 K	400 K	298 K	336 K	400 K	298 K	336 K	400 K
R1+O_2 ⇌ R1-2OO-*syn*	13.17	15.48	18.40	12.32	14.48	17.36	10.65	12.32	14.63	14.06	16.29	19.36
R1+O_2 ⇌ R1-2OO-*anti*	1.34	2.35	4.79	0.75	1.22	2.27	0.13	0.30	0.79	0.17	0.37	0.91
R1+O_2 ⇌ R1-4OO-*syn*	80.40	74.07	62.39	84.39	80.07	72.71	88.02	85.26	80.31	84.44	81.14	75.86
R1+O_2 ⇌ R1-4OO-*anti*	5.09	8.10	14.42	2.54	4.23	7.66	1.20	2.12	4.27	1.33	2.20	3.87

Upon inspecting Figure 6 and Table 9, it is clear that the RRKM effective rate constants obtained from the UM06-2x energy profiles for the R1+O_2⇌R1-*i*OO-*syn/anti* (i=2,4) reaction pathways increase with increasing temperatures. Upon inspecting the RRKM data displayed in Figure 6, it appears quite clearly that, in line with rather larger energy barriers, ranging from 2.7 to 3.8 kcal mol^{-1}, pressures larger than 10^{-2} bar are sufficient for ensuring a saturation within 10 % accuracy of the computed effective kinetic rate constants compared with the high pressure limit. In contrast with our preceding study of the formation of the $[C_{10}H_8OH]^\bullet$ adduct through addition reactions of hydroxyl radicals onto naphthalene,[24] the TST approximation may therefore be regarded as valid at standard temperatures and pressures.

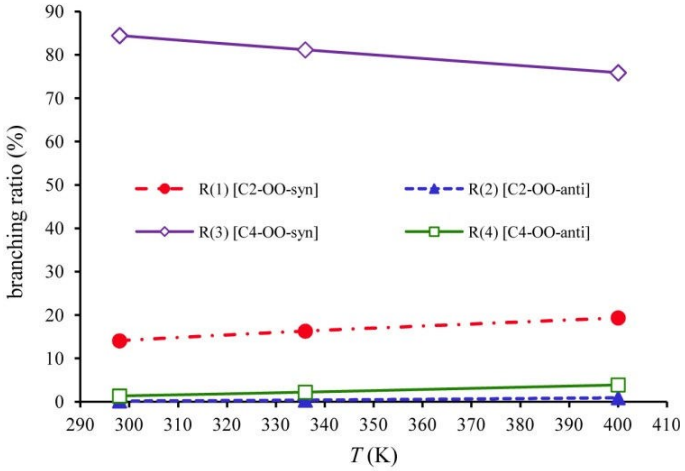

Fig 4. Evaluation of branching ratios in function of the temperature for pathways R1+O_2⇌R1-*i*OO-*syn* (i=2,4) using the UM06-2x/aug-cc-pVTZ approach. Legend: (●) data obtained for the R1+O_2⇌R1-2OO-*syn* pathway; (▲) data obtained for the R1+O_2⇌R1-2OO-*anti* pathway; (◇) data obtained for the R1+O_2⇌R1-4OO-*syn* pathway; (□) data obtained for the R1+O_2⇌R1-4OO-*anti* pathway.

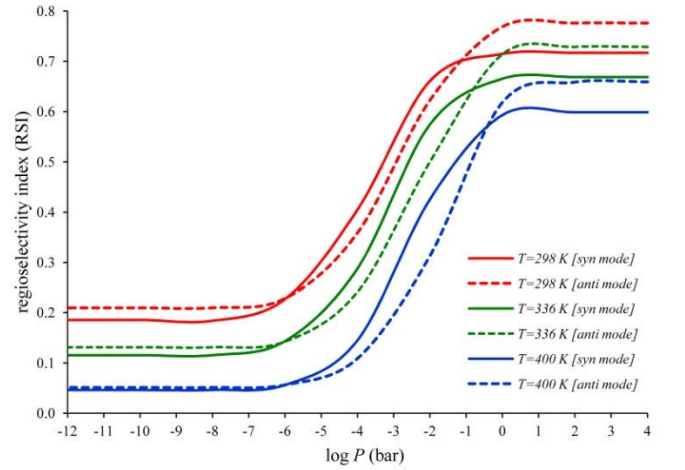

Fig 5. Dependence upon the pressure and temperature of the regioselectivities [RSI =R(**3**)–R(**1**)/R(**1**)+R(**3**)] and [RSI= R(**4**)–R(**2**)/R(**2**)+R(**4**)] of O_2 addition in *syn* and *anti* modes onto the naphthalene-OH adduct $[C_{10}H_8OH]^\bullet$, according to the RRKM estimates of effective rate constants [k_{eff}(**1**), k_{eff}(**2**), k_{eff}(**3**), k_{eff}(**4**)] supplied in Tables S3a–S3f (see Supplementary Information), based on UM06-2x/aug-cc-pVTZ energy profiles.

As anticipated (see end of section 3.1), differences in branching ratios obtained using different theoretical models are all in all quite limited (see Table 10): they do not exceed 4% and 10% at 298 K and 400 K, respectively, which confirms further the relevance and numerical robustness of our analysis.

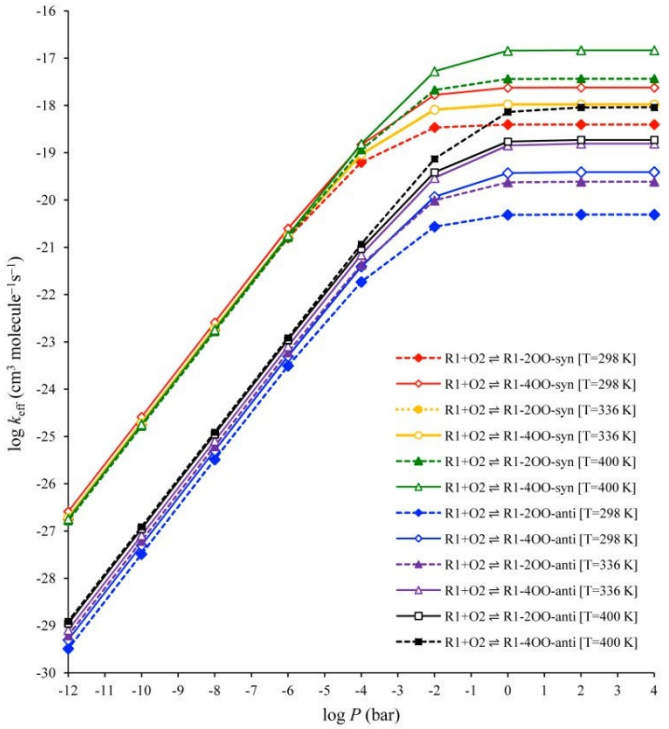

Fig 6. Pressure dependence of the bimolecular rate constants for the R1+O_2⇌R1-*i*OO-*syn/anti* (i=2,4) reaction pathways according to the UM06-2x/aug-cc-pVTZ energy profiles (RRKM results, obtained by means of equations 10–13).

4. Conclusions

The mechanisms for the atmospheric oxidation of naphthalene-OH adduct $[C_{10}H_8OH]^\bullet$ (R1) by molecular oxygen in its triplet electronic ground state have been studied computationally using density functional theory along with various exchange-correlation functional (B3LYP, ωB97XD, UM05-2x and UM06-2x) and an extremely large basis set (aug-cc-pVTZ). All our calculations indicate that, from a thermodynamic viewpoint, the most favourable process is O_2 addition at the C_2 position in *syn* mode, followed by O_2 addition at the C_2 position in *anti* mode, O_2 addition at the C_2 position in *anti* mode, and O_2 addition at the C_4 position in *anti* mode, as the second, third and fourth most favourable processes, respectively. In contrast with recent data by Zhang *et al.*[25], the *syn* modes of addition at the C_2 and C_4 positions appear to be thermodynamically favoured over the *anti* one by the formation of an intramolecular hydrogen bond between the hydroxyl and peroxy substituents. Our study confirms that O_2 additions in C_5, C_7 and C_9 positions are highly unlikely processes, due to unfavourable reaction energies and energy barriers.

A combined structural, energetic and NBO analysis shows that the intramolecular H-bond in the R1-2OO-*syn* radical is stronger than that in the R1-4OO-*syn* radical. Analysis of the computed

structures, bond orders and free energy profiles demonstrates that the reaction steps involved in the oxidation of the naphthalene-OH adduct by O_2 satisfy Hammond's principle: the transition state involved in the formation of the R1-4OO-*syn* radical is structurally closer to the product than the transition state involved in the formation of the R1-2OO-*syn* radical.

The calculated energy profiles have been supplemented with calculations of kinetic rate constants and branching ratios under atmospheric pressure and in the fall-off regime, down to pressure of 10^{-12} bar, using transition state and RRKM theories. The supplied data indicate that, under a kinetic control of the reaction, and in contrast with the situation that prevails at chemical equilibrium (thermodynamic control), the most abundant product resulting from the oxidation of the $[C_{10}H_8OH]^\bullet$ adduct by O_2 must be the R1-4OO-*syn* radical rather than the R1-2OO-*syn* radical. For the *anti* modes as well, O_2 addition in C_4 position is kinetically favoured over addition in C_2 position. Upon considering that O_2 addition in *syn* mode in C_4 position must prevail under a kinetic control of the reaction, the rather excellent agreement between our effective kinetic rate constants with the available experimental ones demonstrates the relevance of the proposed two-step reaction mechanism.[60] The computed branching ratios also indicate that the regioselectivity of the reaction decreases with increasing temperatures and decreasing pressures.

Acknowledgements

A. Shiroudi acknowledges a PhD fellowship from the "Bijzonder Onderzoeksfonds" (BOF) of Hasselt University. All calculations presented in this work have been performed at the Flemish Supercomputer Center (Vlaams Supercomputer Centrum). This cluster has been financed by budgets obtained from the Katholieke Universiteit Leuven, from individual contributions by users, and financing obtained from the Hercules foundation and the Flemish government. Authors would like to acknowledge Prof. J.-P. François for useful discussions.

Notes and references

[a] *Center of Molecular and Materials Modelling, Hasselt University, Agoralaan, Gebouw D, B-3590 Diepenbeek, Belgium. Tel: +32-11-268303; E-mail: michael.deleuze@uhasselt.be*

[b] *Université Lille1 Sciences et Technologies, Cité scientifique, 59655 Villeneuve d'Ascq Cedex, France.*

† Electronic Supplementary Information (ESI) available: Supplementary data (Tables S1–S3) associated with this article can be found, in the online version. Table S1: Effective rate constants (in cm^3 $molecule^{-1}$ s^{-1}) for the reported reaction channels obtained by means of RRKM theory at different pressures and temperatures, according to the computed UM06-2x/aug-cc-pVTZ energy profiles; Table S2: Kinetic rate constants (in s^{-1}), effective rate constants, and branching ratios for all reaction steps involved in the reported chemical pathways at ambient temperature and different pressures using the RRKM theory, according to the computed UM06-2x/aug-cc-pVTZ energy profiles; Table S3: Dependence upon the pressure and temperature of the regioselectivities [RSI=R(**3**)–R(**1**)/R(**1**)+R(**3**)] and [RSI=R(**4**)–R(**2**)/R(**2**)+R(**4**)] of O_2 addition in *syn* and *anti* modes onto the naphthalene-OH adduct $[C_{10}H_8OH]^\bullet$, according to the RRKM estimates of effective rate constants [k_{eff}(**1**), k_{eff}(**2**), k_{eff}(**3**), k_{eff}(**4**)]. See DOI: 10.1039/b000000x/

1. P. T. Williams, M. K. Abbass, G. E. Andrews and K. D. Bartle, *Combust. Flame.,* 1989, **75**, 1.
2. S. K. Hoekman, *Environ. Sci. Technol.,* 1992, **26**, 1206.
3. B. Zielinska, J. Sagebiel, J. D. McDonald, K. Whitney and D. R. Lawson, *J. Air & Waste Manage. Assoc.,* 2004, **54**, 1138.
4. L. C. Marr, T. W. Kirchstetter, R. A. Harley, A. H. Miguel, S. V. Hering and S. K. Hammond, *Environ. Sci. Technol*., 1999, **33**, 3091.
5. M. P. Fraser, G. R. Cass and B. R. T. Simoneit, *Environ. Sci. Technol*., 1998, **32**, 2051.
6. M. Howsam and K. C. Jones, *Handbook of Environmental Chemistry*, Springer-Verlag, Berlin, 1998, **3**, 137.
7. T. F. Bidleman, *Environ. Sci. Technol*., 1988, **22**, 361.
8. F. Wania and D. Mackay, *Environ. Sci. Technol.,* 1996, **30**, 390A.
9. D. G. Hendry and R. A. Kenley, *Atmospheric Reaction Products of Organic Compounds,* U.S. Environmental Protection Agency, EPA-560112-79-001, 1979.
10. R. Atkinson, K. R. Darnall, A. C. Lloyd, A. M. Winer and J. N. Pitts, *Adv. Photochem.*, 1979, **11**, 375.
11. N. J. Bunce, L. Liu and J. Zhu, *Environ. Sci. Technol.*, 1997, **31**, 2252.
12. R. Atkinson and J. Arey, *Environ. Health Perspect.*, 1994, **102**, 117.
13. R. Atkinson, *J. Phys. Chem. Ref. Data, Monograph*, 1989, **1**, 1.
14. R. Atkinson, E. C. Tuazon and J. Arey, *Int. J. Chem. Kinet.*, 1990, **22**, 1071.
15. R. Atkinson, *J. Phys. Chem. Ref. Data, Monograph*, 1991, **20**, 459.
16. R. Atkinson, E. C. Tuazon, I. Bridier and J. Arey, *Int. J. Chem. Kinet.*, 1994, **26**, 605.
17. J. Sasaki, S. M. Aschmann, E. S. C. Kwok, R. Atkinson and J. Arey, *Environ. Sci. Technol.*, 1997, **31**, 3173.
18. K. Lorenz and R. Zellner, *Ber. Bunsen-Ges. Phys. Chem.*, 1983, **87**, 629.
19. R. Atkinson and J. Arey, *Polycyclic Aromat. Compd.,* 2007, **27**, 15.
20. R. Atkinson and J. Arey, *Chem. Rev.,* 2003, **103**, 4605.
21. C. Bloss, V. Wagner, M. E. Jenkin, R. Volkamer, W. J. Bloss, J. D. Lee, D. E. Heard, K. Wirtz, M. Martin-Reviejo, G. Rea, J. C. Wenger and M. J. Pilling, *Atmos. Chem. Phys.,* 2005, **5**, 641.
22. R. Koch, R. Knispel, M. Elend, M. Siese and C. Zetzsch, *Atmos. Chem. Phys.,* 2007, **7**, 2057.
23. A. Shiroudi and M. S. Deleuze, *J. Phys. Chem. A*, 2014, **118**, 3625.
24. A. Shiroudi, M. S. Deleuze and S. Canneaux, *J. Phys. Chem. A*, 2014, **118**, 4593.
25. Z. Zhang, L. Lin and L. Wang, *Phys. Chem. Chem. Phys.*, 2012, **14**, 2645.
26. B. Bohn and C. Zetzsch, *Phys. Chem. Chem. Phys.,* 1999, **1**, 5097.
27. D. Johnson, S. Raoult, M. T. Rayez, J. C. Rayez and R. Lesclaux, *Phys. Chem. Chem. Phys*., 2002, **4**, 4678.
28. S. Y. Grebenkin and L. N. Krasnoperov, *J. Phys. Chem. A,* 2004, **108**, 1953.
29. S. Raoult, M. T. Rayez, J. C. Rayez and R. Lesclaux, *Phys. Chem. Chem. Phys*., 2004, **6**, 2245.
30. B. Bohn, *J. Phys. Chem. A,* 2001, **105**, 6092.
31. R. Koch and C. Zetzsch, *13th International Symposium on Gas Kinetics*, University College Dublin, Ireland, 11–16 September, 1994.
32. R. Koch, R. Knispel, M. Siese and C. Zetzsch, *Physico-Chemical Behaviour of Atmospheric Pollutants*, European Commission, Brussels/ Luxemburg, 1994.
33. C. Zetzsch, R. Koch, B. Bohn, R. Knispel, M. Siese and F. Witte, pp. 247–256 in *Chemical Processes in Atmospheric Oxidation,* edited by G. Le Bras, Springer, Berlin, 1997.
34. R. Koch, B. Bohn and C. Zetzsch, *The Oxidizing Capacity of the Troposphere, Physico-Chemical Behavior of Atmospheric Pollutants*, European Commission, Brussels, 1997.
35. H. Eyring, *J. Chem. Phys.*, 1935, **3**, 107.
36. H. S. Johnston, *Gas Phase Reaction Rate Theory*, Roland Press Co, New York, 1966.
37. K. J. Laidler, *Theories of Chemical Reaction Rates*, McGraw-Hill, New York, 1969.
38. R. E. Weston and H. A. Schwartz, *Chemical Kinetics*, Prentice-Hall, New York, 1972.
39. D. Rapp, *Statistical Mechanics,* Holt, Reinhard, and Winston, New York, 1972.
40. E. E. Nikitin, *Theory of Elementary Atomic and Molecular Processes in Gases*, Claredon Press, Oxford, 1974.
41. I. W. M. Smith, *Kinetics and Dynamics of Elementary Gas Reactions*, Butterworths, London, 1980.
42. J. I. Steinfeld, J. S. Francisco and W. L. Hase, *Chemical Kinetics and Dynamics*, Prentice-Hall, Englewood Cliffs, NJ, 1989.
43. G. Lendvay, *J. Phys. Chem.*, 1989, **93**, 4422.
44. A. E. Reed, L. A. Curtiss and F. Weinhold, *Chem. Rev.*, 1988, **88**, 899.
45. V. Lopez, J. Quijano, S. Luna, P. Ruiz, D. Rios, W. Parra, E. Zapata, J. Gaviria and R. Notario, *Struct. Chem.*, 2013, **24**, 1811.
46. A. D. Becke, *J. Chem. Phys.*, 1993, **98**, 5648.

47. C. Lee, W. Yang and R. G. Parr, *Phys. Rev B*, 1988, **37**, 785.
48. J. D. Chai and M. Head-Gordon, *Phys. Chem. Chem. Phys.,* 2008, **10**, 6615.
49. Y. Zhao and D. G. Truhlar, *Acc. Chem. Res.*, 2008, **41**, 157.
50. Y. Zhao and D. G. Truhlar, *Theor. Chem. Acc.*, 2008, **120**, 215.
51. T. H. Dunning, *J. Chem. Phys.*, 1989, **90**, 1007.
52. A. E. Reed and R. B. Weinstock, *J. Chem. Phys.*, 1985, **83**, 735.
53. J. K. Badenhoop and F. Weinhold, *Int. J. Quantum. Chem*., 1999, **72**, 269.
54. M. J. Frisch, G. W. Trucks, H. B. Schlegel, G. E. Scuseria, M. A. Robb, J. R. Cheeseman, G. Scalmani, V. Barone, B. Mennucci, G. A. Petersson, et al. *Gaussian 09*, Revision B.01; Gaussian, Wallingford, CT, 2009.
55. I. I. R. Dennington, T. Keith, J. Millam, K. Eppinnett, W. L. Hovell and R. Gilliland, *GaussView*, Version 3.09; Semichem, Inc., Shawnee Mission, KS, 2003.
56. C. Gonzalez and H. B. Schlegel, *J. Chem. Phys.*, 1989, **90**, 2154.
57. J. W. Jr. McIver, *Acc. Chem. Res.*, 1974, **7**, 72.
58. F. Fukui, *J. Phys. Chem.*, 1970, **74**, 4161.
59. D. A. McQuarrie, *Statistical Mechanics*, Harper and Row, New York, 1976.
60. G. H. Herzberg, *Molecular Spectra and Molecular Structure. II Infrared and Raman Spectra of Polyatomic Molecules*, Van Nostrand Reinhold, New York, 1945.
61. D. L. Singleton and R. J. Cvetanovic, *J. Am. Chem. Soc.,* 1976, **98**, 6812.
62. R. G. Mortimer, *Physical Chemistry*, 3rd ed., Elsevier Academic Press, Burlington, 2008.
63. R. Chang, *Physical Chemistry for the Biosciences*, University Science Books, Sausalito, California, 2005.
64. J. W. Moore and R. G. Pearson, *Kinetics and Mechanism-The Study of Homogeneous Chemical Reactions*, 3rd ed., Wiley, New York, 1981.
65. H. H. Carstensen, A. M. Dean and O. Deutschmann, *Proc. Combust. Inst.*, 2007, **31**, 149.
66. D. H. Varma, P. Raghunath and M. C. Lin, *J. Phys. Chem. A*, 2010, **114**, 3642.
67. S. Y. Wu, P. Raghunath, J. S. Wu and M. C. Lin, *J. Phys. Chem. A*, 2010, **114**, 633.
68. R. G. Gilbert and S. C. Smith, *Theory of Unimolecular and Recombonitation Reactions*, Blackwell Scientific, Oxford, 1990.
69. H. B. Rao, X. Y. Zeng, H. He and Z. R. Li, *J. Phys. Chem. A*, 2011, **115**, 1602.
70. S. Canneaux, F. Bohr and E. Henon, *J. Comput. Chem.*, 2014, **35**, 82.
71. F. Rosas, R. M. Dominguez, M. Tosta, J. R. Mora, E. Marquez, T. Cordova and G. Chuchani, *J. Phys. Org. Chem.*, 2010, **23**, 743.
72. E. A. Mason and L. Monchick, *Humidity and Moisture Measurement and Control in Science and Industry. Survey of the Equation of State and Transport Properties of Moist Gases,* Rheinhold Publishing Corp, New York, 1965.
73. J. B. Chaddock, *Moist Air Properties from Tabulated Virial Coefficients. Humidity and Moisture Measurement and Control in Science and Industry*, Reinhold Publishing Corp, New York, 1965.
74. Y. Iwai, H. Higashi, H. Uchida and Y. Arai, *Fluid Phase Equilib*., 1997, **127**, 251.
75. I. García-Cruzl, M. Castro and A. Vivier-Bunge, *J. Comput. Chem.,* 2000, **21**, 716.
76. G. E. Scuseria and H. F. Schaefer III, *J. Chem. Phys.,* 1989, **90**, 3629.
77. R. S. Grev and H. F. Schaefer III, *J. Chem. Phys.,* 1989, **91**, 7305.
78. M. Huang, Z. Wang, Y. Yang, L. HAO, W. Zhao, X. Gao, L. Fang and W. Zhang, *Int. J. Quantum. Chem.*, 2007, **107**, 1092.
79. N. Agmon and R. D. Levine, *Chem. Phys. Lett.*, 1977, **52**, 197.
80. J. E. Carpenter and F. Weinhold, *J. Mol. Struct.(THEOCHEM)*, 1988, **169**, 41.

